



Article

In Situ Synthesis of Ag@Cu₂O-rGO Architecture for Strong Light-Matter Interactions

Shuang Guo ^{1,2}, Yaxin Wang ^{1,*}, Fan Zhang ¹, Renxian Gao ¹, Maomao Liu ¹, Lirong Dong ¹, Yang Liu ², Yongjun Zhang ^{2,*} and Lei Chen ^{3,*}

¹ College of Physics, Jilin Normal University, Siping 136000, China; guoshuang0420@163.com (S.G.); zhangfan147258@126.com (F.Z.); ren7771993@163.com (R.G.); 18844592029@163.com (M.L.); dlr5640@163.com (L.D.)

² Key Laboratory of Functional Materials Physics and Chemistry, Ministry of Education, Jilin Normal University, Changchun 130103, China; liuyang@jlnu.edu.cn

³ College of Chemistry, Jilin Normal University, Siping 136000, China

* Correspondence: wangyaxin1010@126.com (Y.W.); yjzhang@jlnu.edu.cn (Y.Z.); chenlei@jlnu.edu.cn (L.C.); Tel./Fax: +86-434-329-4566 (Y.Z.)

Received: 10 May 2018; Accepted: 12 June 2018; Published: 17 June 2018



Abstract: Emerging opportunities based on two-dimensional (2D) layered structures can utilize a variety of complex geometric architectures. Herein, we report the synthesis and properties of a 2D+0D unique ternary platform-core-shell nanostructure, termed Ag@Cu₂O-rGO, where the reduced graphene oxide (rGO) 2D acting as a platform is uniformly decorated by Ag@Cu₂O core-shell nanoparticles. Cu₂O nanoparticles occupy the defect positions on the surface of the rGO platform and restore the conjugation of the rGO structure, which contributes to the significant decrease of the I_D/I_G intensity ratio. The rGO platform can not only bridge the isolated nanoparticles together but also can quickly transfer the free electrons arising from the Ag core to the Cu₂O shell to improve the utilization efficiency of photogenerated electrons, as is verified by high efficient photocatalytic activity of Methyl Orange (MO). The multi-interface coupling of the Ag@Cu₂O-rGO platform-core-shell nanostructure leads to the decrease of the bandgap with an increase of the Cu₂O shell thickness, which broadens the absorption range of the visible light spectrum.

Keywords: nanocomposite; rGO-substrate; Ag@Cu₂O; interfacial effect

1. Introduction

Since Geim and Novoselov discovered the two-dimensional (2D) electron motion in graphene, 2D materials have attracted attention due to their unique properties and their wide applications in photocatalysis, sensing, detection, and energy storage [1–8]. In recent years, researchers have conducted in-depth explorations of 2D materials to create a large 2D family of materials that mainly include carbon nanomaterials, metal oxides, transition metal dichalcogenides, hexagonal boron nitride, and so on [9–13]. Two-dimensional graphene composing of carbon atoms has attracted high attention due to its excellent physical properties, such as ballistic transport, high Young's Modulus, and super-high electron mobility. However, the zero-band system properties of graphene prevented it from being directly used in optoelectronic devices and photocatalytic processes which were based on the utilization of carriers. To overcome the limitation of graphene, synergistic effects were recommended by using carboxylic acid groups [14], semiconductors, or noble metal composites [15]. To date, a series of graphene-based composites have been realized, for example, a semiconductor and graphene oxide composite (TiO₂/GO) [16], noble metal and graphene oxide composite (Ag/GO) [17], hydroxide and graphene oxide composite (Zn(OH)₂/GO) [18], and multiple structure composite

(Ag-ZnFe₂O₄@rGO) [19]. These graphene-based composites have excellent electron transport channels and can quickly transfer excitons to suppress the recombination of carriers compared to other carbon nanomaterials [20,21]. Although the synergistic effects bring some advantages, they also undermine the low-dimensional structure of the graphene and it is still difficult to modify the nanostructure system on the surface of 2D graphene, especially the core-shell heterostructure arranged on the surface of graphene. Therefore, it is necessary to create a new composite structure which can not only keep the graphene low-dimensional structure but also connect the isolated nanostructure units together.

Guo et al. reported the ternary Ag-Cu₂O/rGO with excellent peroxidase-like nanocatalysts, which was based on the Cu₂O sphere modified by Ag nanoparticles and attached to rGO [22]. However, the surface of Ag nanoparticles are not stable. To overcome the instability of surface Ag nanoparticles, we designed a heterostructure of Ag@Cu₂O-reduced graphene oxide with the core-shell complex-structure. Ag@Cu₂O core-shell nanoparticles are considered excellent photocatalytic candidate material, which have excellent performance in photocatalytic degradation of pollutants [23]. The main reasons to use Cu₂O as a shell structure are: (1) Cu₂O has a narrow bandgap (2.2 eV) compared with a wide bandgap semiconductor (like ZnO) [24], in which the absorption band is located in the visible light range; (2) Cu₂O has advantages of excellent catalytic efficiency for C-C, C-N, and C-O bonds. Ag can provide plenty of free electrons and the large energy level difference between the Ag nanoparticles and Cu₂O facilitates the transfer of photogenerated electrons between the Cu₂O shell and the Ag core [25,26]. However, the increase of carrier efficiency in a pure core-shell structure is limited, and composite materials with higher efficiencies are still required. Therefore, combining the Ag@Cu₂O core-shell structure with graphene, which is a superior electron transport material, can both improve the utilization of sunlight and achieve higher carrier transfer efficiency.

In this paper, this was the first time to report the orderly arrangement of Ag@Cu₂O core-shell structures on an rGO substrate. The rGO nanosheets act as a sheet platform and the Ag@Cu₂O core-shell nanoparticles are decorating the surface of the rGO, which forms a 2D+0D heterogeneous structure. The broad spectral absorption and enhanced charge transfer efficiency in the Ag@Cu₂O-rGO platform-shell-nucleus configuration have been observed. We demonstrated that the structure has strong light-matter interactions using photocatalytic degradation of the Methyl Orange (MO). Our study indicates that the Ag@Cu₂O-rGO platform-shell-core configuration with wide spectral absorption and strong light-matter interactions is a new candidate to be applied in photoanodes, photoelectrocatalysis, and so on.

2. Experimental Section

2.1. Materials

Potassium persulfate (K₂S₂O₈, AR, Shanghai China), phosphorus pentoxide (P₂O₅, AR, Shanghai China), graphite powder, concentrated sulfuric acid (H₂SO₄, 98.98 wt %, Shanghai China), potassium permanganate (KMnO₄, Shanghai China), phosphoric acid (H₃PO₄, 85 wt %, Shanghai China), hydrogen peroxide (H₂O₂, 30 wt %, Shanghai China), silver nitrate (AgNO₃, AR, Shanghai China), sodium citrate dihydrate (C₆H₅-Na₃O₇·2H₂O, AR, Shanghai China), copper(II) nitrate trihydrate (Cu(NO₃)₂·3H₂O, AR, Shanghai China), polyvinylpyrrolidone (C₆H₉NO) n, AR, Shanghai China) and we named as PVP, hydrazine hydrate (H₄N₂·H₂O, 85 wt %, Shanghai China), and anhydrous ethanol (C₂H₆O, ≥ 99.8 wt %, Beijing, China) were purchased from Sinopharm Chemical Reagent Co., Ltd. All chemicals were used as received without further treatment. Deionized water was used in all solution preparations in this study.

2.2. Preparation of the Ag@Cu₂O-rGO Composites

2.2.1. Fabrication and Modification of a 2D Graphene Oxide (GO) Nanosheet

GO nanosheets were synthesized by a two-step oxidation of graphite powder summarized from Hummer's and Offeman's method [27]. Then, the surface of the GO sheet was modified with Ag nanoparticles (NPs). First, 1 mg of GO was dispersed in 30 mL of deionized water, and the solution was sonicated for 1 h to obtain homogeneously dispersed GO. The GO solution and 170 mL of deionized water were poured into a three-necked flask, and the solution was uniformly dispersed by magnetic stirring. Then, 36 mg of AgNO₃ was added to the three-necked flask and slightly boiled at 90 °C for 20 min. Finally, 4 mL of a sodium citrate dihydrate (C₆H₅-Na₃O₇·2H₂O, 1 wt %) solution was added quickly to the flask, and the solution was incubated at 85 °C for 30 min until the solution became dark green. The Ag-rGO composite structure based on graphene oxide was obtained.

2.2.2. Synthesis of the Ag@Cu₂O-rGO Composites

To get the Ag@Cu₂O-rGO structure, our previous synthesis method of Ag@Cu₂O core-shell structure was improved [28]. The specific method is as follows: 50 mL of 8 mM Cu(NO₃)₂ solution was poured into a beaker. Then, 1 g PVP was added to the Cu(NO₃)₂ solution, and the solution was magnetically stirred for 5 min to completely dissolve the PVP. Twenty milliliters of the as-prepared Ag-GO solution were centrifuged, washed, and dispersed in the Cu(NO₃)₂ solution. Fifty-five microliters of H₄N₂·H₂O (35 wt %) were added to the beaker, and the solution was continuously magnetically stirred (300 rpm) and maintained for 90 s at room temperature. Then, the Ag@Cu₂O-rGO composite structures formed. Finally, the composite structures were centrifuged, washed, and stored in centrifuge tubes (4 °C). Change the concentration of Cu(NO₃)₂ (0 mM, 2 mM, 4 mM, 6 mM, 8 mM, and 10 mM) and the added volume of H₄N₂·H₂O (0, 14, 27, 41, 55, and 68 μL) in the above experiment to acquire a group of Ag@Cu₂O-rGO composite structures containing different Cu₂O ratios.

2.3. Degradation MO Experiments

The photocatalytic activity of the materials was tested under visible-light irradiation at room temperature using MO as the probe molecule. The detailed steps are as follows. First, 1 mg of the sample was uniformly dispersed in 50 mL of an MO solution (4 mg/L). Then, the material was allowed to adsorb the dye under dark conditions for 40 min to reach adsorption equilibrium before visible-light irradiation. Under constant visible-light irradiation, 2 mL of the mixed solution was removed from the above solution at regular intervals, and the 2 mL sample was centrifuged at 10,000 rpm for 3 min. The absorbance of the resulting supernatant was tested using a Hitachi U-4100 spectrophotometer (Hitachi, Tokyo, Japan). Finally, the initial and final concentrations of the solution were used to calculate the degradation efficiency of MO by the following equation:

$$D\% = (c_0 - c_t)/c_0 \times 100\%$$

where c_0 is the MO initial concentration, and c_t is the temporal concentration of MO.

2.4. Characterization

Scanning electron microscopy (SEM, JEOL Ltd., Tokyo, Japan) images were obtained by using a JEOL 7800F scanning electron microscope operated at a 5.0 kV accelerating voltage to study the surface morphologies of the samples. Transmission electron microscopy (TEM, JEOL Ltd., Tokyo, Japan) images were obtained by using a Hitachi H-800 transmission electron microscope operated at a 200-kV accelerating voltage to study the crystallization of the nanomaterials. X-ray photoelectron spectroscopy (XPS, Thermo Fisher Scientific, Waltham, MA, USA) was performed by using Thermo Fisher Scientific system to study the elemental composition and chemical state of the samples. UV-Vis (Tokyo, Japan) absorption spectra were obtained by using a Shimadzu 3600 spectrometer to study

the optical properties of the structures. The absorption spectra were obtained by a Hitachi U-4100 spectrophotometer to study the concentration of the signal molecule.

3. Results and Discussion

3.1. Structure and Properties of the Ag@Cu₂O-rGO Nanocomposites

Figure 1 shows the fabrication process for the Ag@Cu₂O-rGO platform-shell-core structure. First, GO nanosheets acting as the platform for Ag NPs were synthesized by a two-step oxidation of graphite powder. Then, Ag NPs were decorated on the GO nanosheets based on the sol-gel method. Finally, Cu₂O was reduced in situ on the Ag NP's surface. The detailed fabrication process is given in Section 2.2 and Figure S1. Figure 2A–F shows the SEM images of the platform-shell-core Ag@Cu₂O-rGO prepared by reducing Cu(NO₃)₂ with different concentrations: 0 mM, 2 mM, 4 mM, 6 mM, 8 mM, and 10 mM, and the samples are labeled as S-0 mM, S-2 mM, S-4 mM, S-6 mM, S-8 mM and S-10 mM, respectively. It can be seen from Figure 2 that all of the samples were decorated by the Ag@Cu₂O nanoparticles on the micron scale. In addition, the nanoparticles distribute dispersedly on the sheet without obvious agglomeration. Compared to the SEM image of the single GO (Figure S2), the composite Ag@Cu₂O-rGO show a 2D structure, which indicates that rGO acts as the stable platform for the modification of Ag@Cu₂O. The sizes of the Ag@Cu₂O nanoparticles on platform rGO gradually increase as the concentrations of Cu(NO₃)₂ increase from 0 mM to 10 mM, as shown in the SEM images. The inset TEM images also show some obvious small Cu₂O nanoparticles on the surface of Ag when the Cu(NO₃)₂ is added, and the perfect shell-core structure of the nanoparticles is found when the concentration of Cu(NO₃)₂ is higher than 6 mM, and the thickness of the shell increases from 10 ± 2 nm for S-6 mM to 13 ± 2 nm for S-10 mM, respectively, but the size of core remains unchanged at about 14 ± 3 nm as shown in the Figure S3.

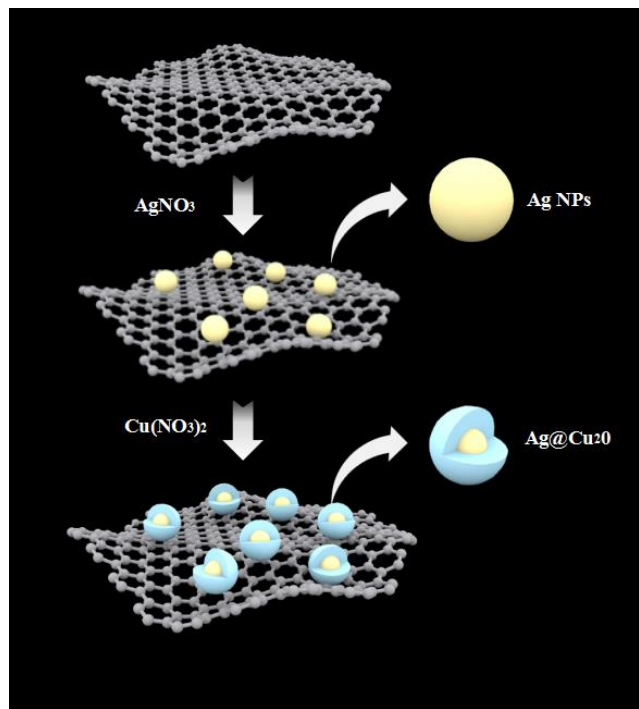


Figure 1. Schematic of the synthetic procedure for Ag@Cu₂O-reduced graphene oxide (rGO) nanostructures.

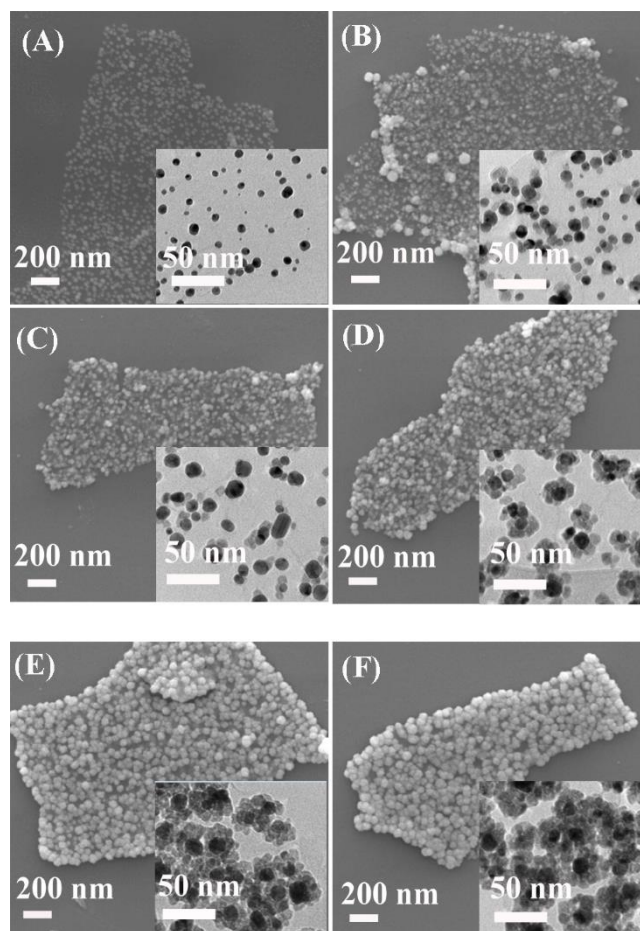


Figure 2. SEM images of (A) Ag-rGO and Ag@Cu₂O-rGO nanocomposites with different concentrations of Cu(NO₃)₂ solution ((B–F), S-2 mM, S-4 mM, S-6 mM, S-8 mM, and S-10 mM). The insets are the corresponding TEM images.

High resolution transmission electron microscopy (HRTEM) measurement in Figure 3A,B is used for Ag@Cu₂O-rGO prepared from Cu(NO₃)₂ concentration 8 mM (S-8 mM). The interplanar spacing of the core is 0.244 nm corresponding to the (111) plane of cubic Ag, and the interplanar spacing of shell is about 0.285 nm corresponding to the (200) plane of cubic Cu₂O, as in Figure S4, X-ray diffraction patterns can further explain the types of elements contained in the structure, as in Figure S5. The energy dispersive spectrometer (EDS) profile (Figure 3C) shows four elements of C, O, Ag, and Cu, and the corresponding line profile (Figure 3D) shows the Ag line profile (green line) is obviously smaller than the line profile of Cu (blue line), indicating that the Cu₂O shell has been modified and encapsulated by the Ag nanoparticles. The EDS mapping of the Ag@Cu₂O-rGO nanocomposite is shown in Figure S6. It was observed that the C content in the sample area is significantly higher than in the surrounding area, thus indicating that the Ag@Cu₂O core-shell structure is grown on rGO. The typical XPS survey scan spectra in Figure 4A confirm the Cu presence in addition to C, Ag, and O elements when Ag-rGO is decorated by Cu₂O. The intensity of the Ag peaks in Ag@Cu₂O-rGO decrease in comparison with that of Ag-rGO, which confirms further that the Ag nanoparticles are covered by Cu₂O [29]. XPS spectra of C 1s for Ag-rGO and Ag@Cu₂O-rGO in Figure 4B,C are deconvoluted into five carbon peaks centered at 284.6, 285.6, 286.0, 287.6, and 288.8 eV, which are assigned to sp²-hybridized carbon (C=C), sp³-hybridized carbon (C–C), hydroxyl carbon (C–O), carbonyl carbon (C=O), and carboxyl carbon (O=C–O), respectively [27]. Compared with Ag-rGO, the intensities of the C–O and C–C peaks decrease for Ag@Cu₂O-rGO. We speculate that the hydroxyl in graphene is replaced by the newly synthesized Cu₂O nanoparticles and the conjugated graphene networks are re-established.

The characteristic peaks of Cu 2p_{3/2} and Cu 2p_{1/2} at 932.8 eV and 952.8 eV position are assigned to Cu⁺ and without other peaks are observed in the Figure 4D [30]. This result indicates that all Cu elements in the Ag@Cu₂O-rGO exist in the form of Cu₂O. In Figure 4E, the peaks of Ag3d at 367.6 (Ag 3d_{5/2}) and 373.5 eV (Ag 3d_{3/2}) in Ag@Cu₂O-rGO move to a higher binding energies position than that of Ag3d in Ag-rGO, which is caused by the transfer of free electrons on the Ag surface [22]. For the Ag@Cu₂O-rGO platform-shell-core structure, rGO with a better conductivity property acts as an electron transfer platform so that it quickly transfers the free electrons on the Ag surface to the Cu₂O shell or adjacent core-shell structure.

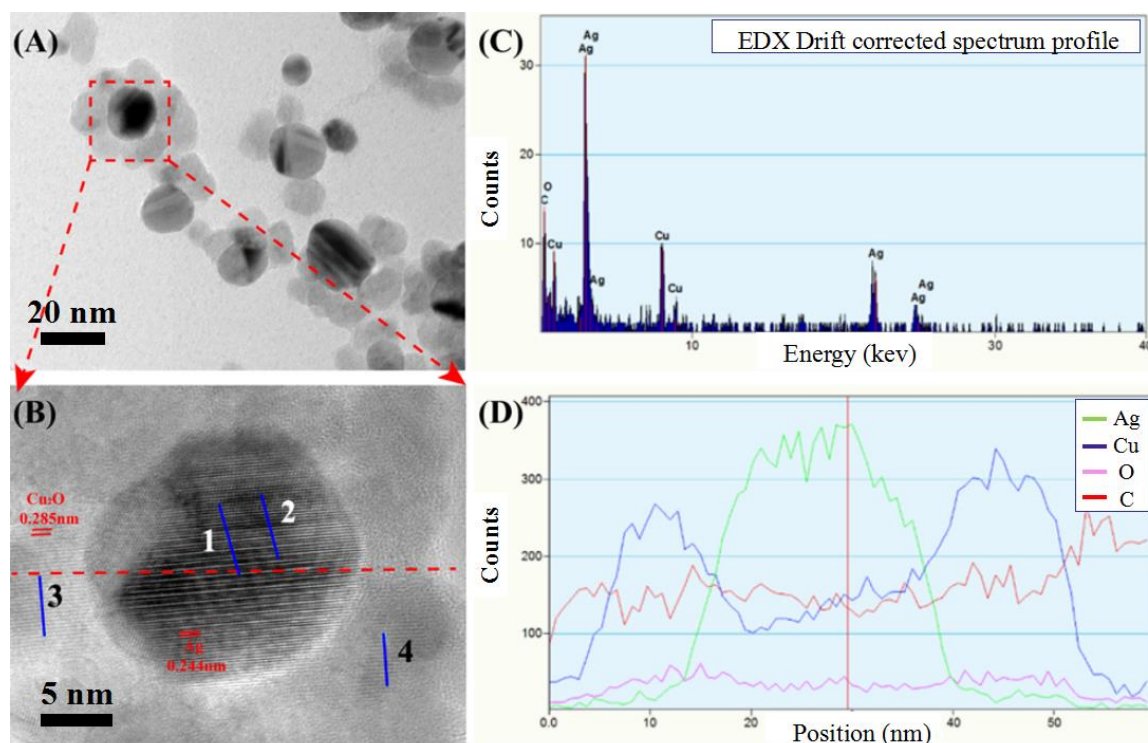


Figure 3. TEM image (A) and high-resolution TEM image (B) of the Ag@Cu₂O-rGO (S-8 mM). The EDS line on the red segment in (B) corresponds to the different elements (C) and the corresponding element count-position curve (D).

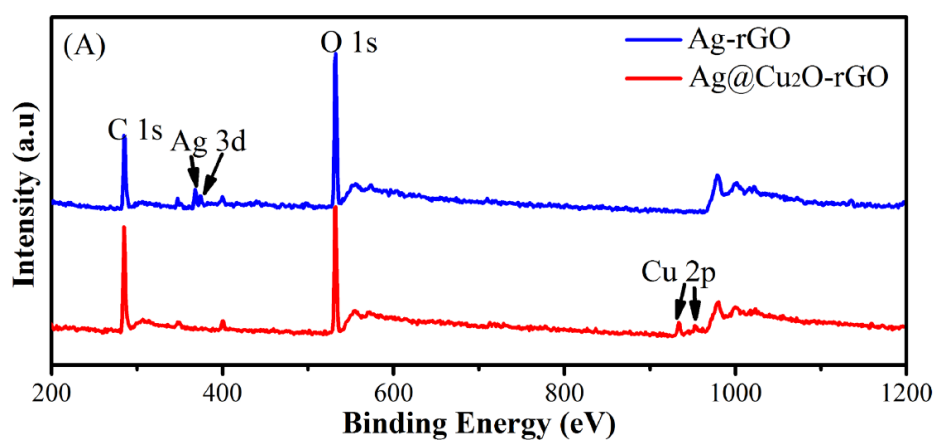


Figure 4. Cont.

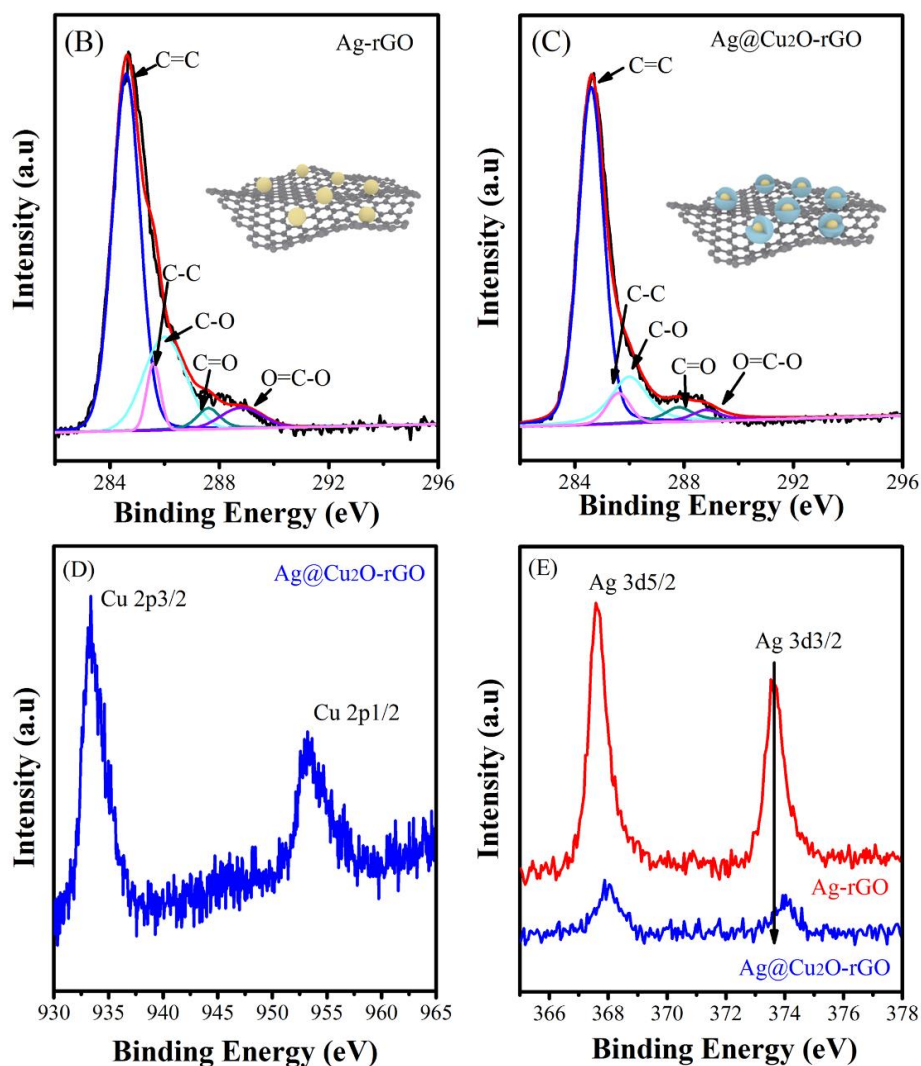


Figure 4. The X-ray photoelectron spectroscopy (XPS) survey spectra (A) of Ag-rGO and Ag@Cu₂O-rGO; high-resolution XPS spectra of C 1s for (B) Ag-rGO and (C) Ag@Cu₂O-rGO. The XPS survey spectra of Cu element and Ag element (D) in Ag@Cu₂O-rGO.

Figure 5A shows the Raman spectra of GO, Ag-rGO, and Ag@Cu₂O-rGO. The Raman spectra showed two characteristic bands centered at 1353 cm⁻¹ (D band) and 1587 cm⁻¹ (G band) for graphitic domains. The D band is the defect band, which is based on the presence of sp³ hybridized carbon (C–C) atoms. The stretching vibration of the sp² hybridized C=C bond is the main reason for the G band. The ratio of the Raman intensity (I_D/I_G) is usually calculated for the disorder degree of the GO [31]. According to the spectra in Figure 5A, the I_D/I_G values of the GO and Ag-rGO and Ag@Cu₂O-rGO are calculated to be 0.93, 0.95, and 0.79, respectively. Compared with GO, the I_D/I_G increases slightly when Ag is decorated on rGO (that is Ag-rGO) while I_D/I_G decreases significantly in Ag@Cu₂O-rGO. It is believed that the increase of I_D/I_G is caused by the increase of defect when GO is reduced to rGO by sodium citrate in the Ag-rGO formation process [32]. However, when Cu₂O is introduced to the Ag-rGO system to form the Ag@Cu₂O-rGO structure, Cu₂O NPs on the surface of the rGO platform occupied the defect position of rGO and restored the conjugation of rGO platform, which contributes to the significant decrease of the I_D/I_G intensity ratio. This result also confirms the speculation in XPS analysis. The Fourier transform infrared (FT-IR) spectra also can indicate that most of the oxygen-containing groups in GO have been removed by two reduction reactions in the complex, as in Figure S7. Figure 5B shows the Raman spectra of Ag@Cu₂O-rGO platform-core-shell

structure for different samples (S-2mM to S-10mM). The peaks at 283 and 619 cm^{-1} are assigned to Cu_2O and the relative intensity increases when the Cu_2O thickness increases. The G band of rGO shifts to a higher frequency with the increase of Cu_2O thickness and the peaks center at 1587, 1588, 1603, 1605, and 1605 cm^{-1} for $\text{Ag}@Cu_2O$ -rGO samples S-2mM to S-10mM, as shown in the inset of Figure 5B. This result confirms the charge is transferred from rGO to Cu_2O . It is known that the rGO cannot generate free electrons by itself but can transfer electrons [33]. Combining with the XPS result of Ag, the peak shift of rGO is caused by the charge transfer between the Ag core and the Cu_2O shell. In the $\text{Ag}@Cu_2O$ -rGO, rGO acts as an electron transfer platform to make the free electrons on the Ag surface via rGO to the Cu_2O shell accompanied by peaks shift of G band.

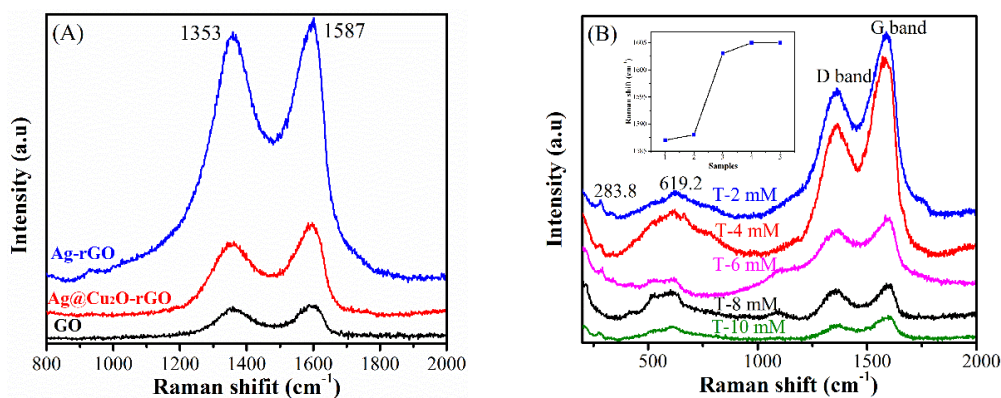


Figure 5. (A) Raman spectra of GO, Ag-rGO, and $\text{Ag}@Cu_2O$ -rGO; (B) Raman spectra of $\text{Ag}@Cu_2O$ -rGO nanocomposites for S-2 mM to S-10 mM, the inset shows the dependence of the intensity of $\text{Ag}@Cu_2O$ -rGO on Cu_2O content.

3.2. Optical Properties of the $\text{Ag}@Cu_2O$ -rGO Nanocomposites

The spectral absorption of nanomaterials reflects the light response of the material directly, and the optical properties of the $\text{Ag}@Cu_2O$ -rGO are characterized by UV-VIS absorption spectroscopy. Figure 6A shows UV-VIS absorption spectroscopy of $\text{Ag}@Cu_2O$ -rGO for samples S-0 mM to S-10mM. Without Cu_2O shell, the Ag-rGO samples display two significant bands, the band in the range of 250–320 nm arising from the $\pi \rightarrow \pi^*$ transition of the C=C bands and the $n \rightarrow \pi^*$ transition of the C=O bonds in rGO, and the band in the range of 320–500 nm arising from the surface plasmon resonance (SPR) of Ag NPs [34]. When the amount of Cu_2O is increased, the absorption peak of $\text{Ag}@Cu_2O$ core-shell structure appears gradually at 500–650 nm and the absorption edge shows an obvious red shift with the thickness of the Cu_2O increases. The SPR band of the silver nanoparticles also shows a significant red shift due to the interfacial effect between the Cu_2O nanoparticles and the Ag nanoparticles. The band gap of the sample can be roughly calculated based on the relationship between the incident light energy and the absorption coefficient in the band theory [35]. The bandgaps for the $\text{Ag}@Cu_2O$ -rGO samples S-0 mM to S-4 mM are approximately 2.22, 2.12, and 1.90 eV, when the core-shell structure is formed (S-6 mM), the composite structure shows longer wavelength absorbance and the band energy is significantly reduced, as displayed in Figure 6B. The bandgap of the $\text{Ag}@Cu_2O$ -rGO gradually decreases as the Cu_2O thickness increases, and the optimum bandgap value of 1.71 eV (S-6 mM) was determined. The decreasing of bandgap is attributed to the Schottky effect of Cu_2O and Ag and the multi-interface coupling in $\text{Ag}@Cu_2O$ -rGO composites. However, the abnormal small increasing of bandgap for the $\text{Ag}@Cu_2O$ -rGO (S-10 mM) is caused by the excess content of Cu_2O that is not affected by the interface effect.

The photo-substance interaction ability of the $\text{Ag}@Cu_2O$ -rGO nanocomposites are evaluated by examining the photocatalytic degradation of an MO (4 mg/L) aqueous solution with visible-light irradiation, as shown in Figure 7A. The change in the amount of MO in an aqueous solution is monitored by detecting the maximal absorption in the UV-VIS spectra at 463 nm, as shown in Figure 7B.

The degradation percentages of Ag-rGO and Ag@Cu₂O-rGO with different Cu₂O shell thicknesses are S-8 mM (94.0%) > S-10 mM (90.3%) > S-6 mM (43.0%) > S-4 mM (6.3%) \approx S-2 mM (6.2%) > S-0 mM (3.0%). Obviously, the photocatalytic activity of Ag@Cu₂O-rGO dramatically increases as the Cu₂O thickness increases from 0 mM to 8 mM and the optimum photocatalytic activity is obtained by S-8 mM. Comparison of catalytic performance of Ag@Cu₂O-rGO and Ag@Cu₂O structures showed that Ag@Cu₂O-rGO (S-8 mM)'s catalytic ability is better than Ag@Cu₂O as shown in Figure S8. Analysis of the catalytic mechanism of Ag@Cu₂O-rGO nanocomposites is based on photocatalytic theory of semiconductors and metals, and the unique nature of the structure as depicted in Figure 8. In Ag@Cu₂O core-shell, the semiconductor of Cu₂O energizes the photogenerated electron-hole pairs under illumination of light with energy greater than 1.71 eV. The electrons transfer from the conduction band of Cu₂O to the Fermi level of the Ag NPs leaving holes in the valence band of Cu₂O, since the work function of Ag is 4.26 eV which is lower than Cu₂O (~5.0 eV) [36]. Based on the unique nature of the Ag@Cu₂O-rGO nanocomposites, the vibrational frequency of the G band moved to high frequencies when Cu₂O particles was introduced to the system, which indicates that electrons move from rGO to Cu₂O. Therefore, the rGO as the charge-transfers platform makes the electrons transfer quickly from Ag NPs to the Cu₂O shell layer or adjacent core-shell structure to increase photon utilization efficiency. The results above indicate that the Ag@Cu₂O-rGO platform-core-shell nanocomposite has an excellent light-matter interaction.

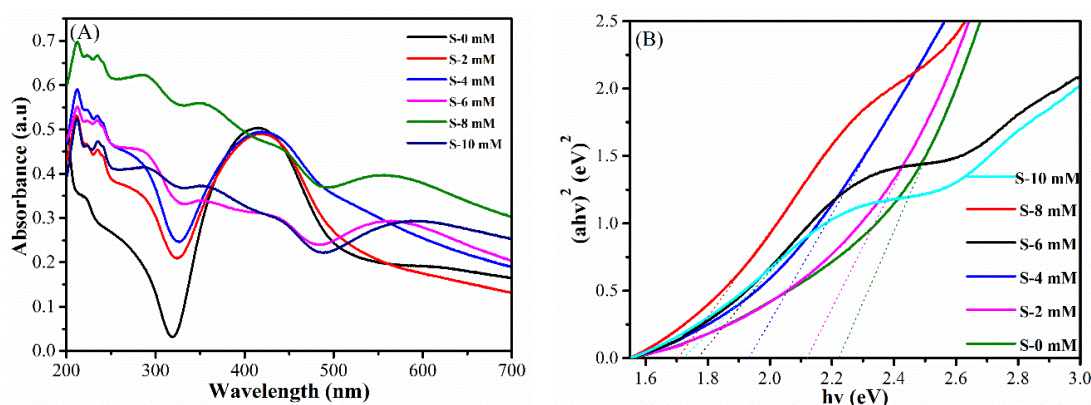


Figure 6. (A) UV-VIS absorption spectra of Ag-rGO and the Ag@Cu₂O-rGO nanocomposites S-2 mM, S-4 mM, S-6 mM, S-8 mM, and S-10 mM; (B) the plots of $(\alpha h\nu)^2$ vs. photon energy ($h\nu$).

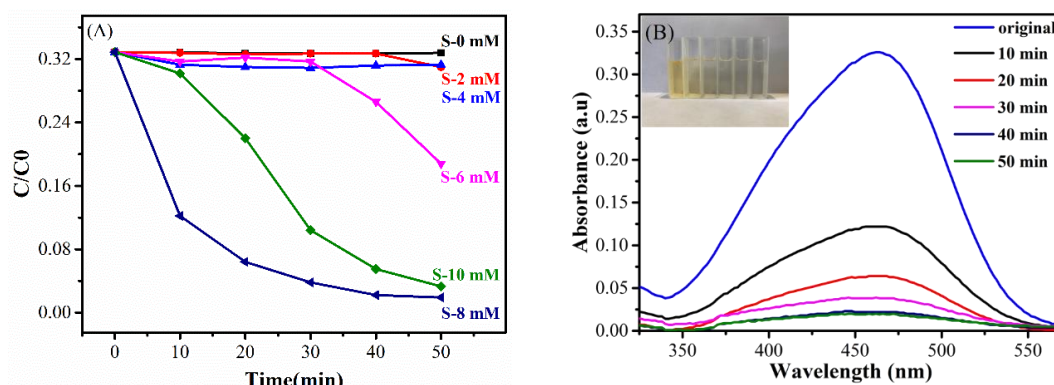


Figure 7. (A) Photocatalytic degradation of Methyl Orange (MO) (4 mg/L) under visible-light irradiation at room temperature with different catalysts: Ag-rGO and the Ag@Cu₂O-rGO nanocomposites S-2 mM, S-4 mM, S-6 mM, S-8 mM, and S-10 mM; (B) absorption spectra of the photocatalytic degradation of MO in the presence of Ag@Cu₂O-rGO (S-8 mM) the inset is the corresponding digital camera photographs of MO dye.

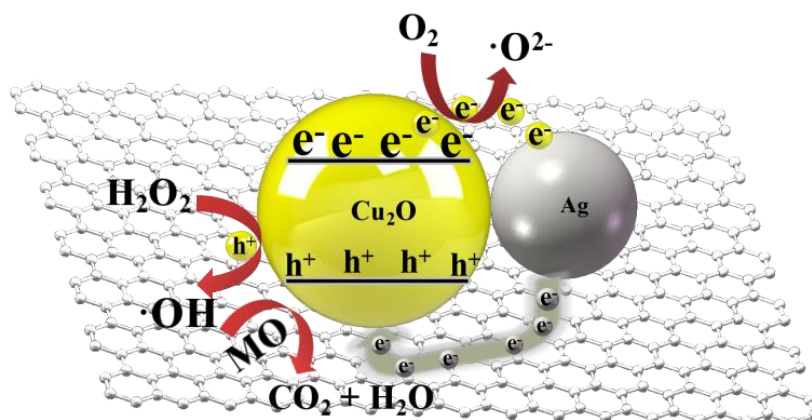


Figure 8. Schematic illustration of the Ag@Cu₂O-rGO charge transfer in the photocatalytic degradation process of MO.

4. Conclusions

In summary, we designed a heterostructure of Ag@Cu₂O-reduced graphene oxide (rGO) with the core-shell complex-structure. The rGO nanosheets act as a sheet platform and the Ag@Cu₂O core-shell nanoparticles are decorating the surface of the rGO, which forms a 2D+0D heterogeneous structure. Cu₂O nanoparticles occupy the defect positions on the surface of the rGO platform and restore the conjugation of the rGO structure, which contributes to the significant decrease of the I_D/I_G intensity ratio. The rGO platform can not only bridge the isolated nanoparticles together but also can quickly transfer the free electrons arising from the Ag core to the Cu₂O shell to improve the utilization efficiency of photogenerated electrons. The broadened absorption of visible light and high efficient photocatalytic activity to MO in Ag@Cu₂O-rGO indicates the strong light–matter interactions.

Supplementary Materials: The following are available online at <http://www.mdpi.com/2079-4991/8/6/444/s1>, Figure S1: Schematic flow chart of the synthetic procedure for Ag@Cu₂O-rGO nanostructures, Figure S2: SEM image of GO, Figure S3: Particle size distribution (A) Internal Ag NPs diameter of S-6 mM; (B) External Cu₂O shell thickness of S-6 mM; (C) Internal Ag NPs diameter of S-10 mM; (D) External Cu₂O shell thickness of S-10 mM, Figure S4: the drawing of crystal surface spacing correspond to HRTEM in Figure 1C, Figure S5: X-Ray diffraction patterns of GO, Ag-rGO and Ag@Cu₂O-rGO, Figure S6: EDS elemental mapping images (C, Cu and Ag) of corresponding red line square for Ag@Cu₂O-rGO nanocomposites, Figure S7: FTIR spectra of GO and Ag@Cu₂O-rGO, Figure S8: Photocatalytic degradation of MO (4 mg/L) under visible-light irradiation at room temperature with different catalysts: Ag@Cu₂O and the Ag@Cu₂O-rGO(S-8 mM) nanocomposites.

Author Contributions: S.G. designed the experiments, analyzed the data, and wrote the article; Y.W., L.C., Y.Z., L.D., and Y.L. discussed the results; M.L., F.Z., and R.G. performed the experiments and processed data; all authors discussed the results and commented on the manuscript.

Funding: This research received no external funding.

Acknowledgments: This work is supported by the National Natural Science Foundation of China (No. 61575080, 61675090 and 21676115), National Youth Program Foundation of China (No. 21546013, 61405072 and 51609100), Program for the Development of Science and Technology of Jilin province (No. 20150519024JH, and 20160101287JC), and Technology of Education Department of Jilin Province (JJKH20170374KJ).

Conflicts of Interest: The authors declare no conflict of interest.

References

- Novoselov, K.S.; Geim, A.K.; Morozov, S.V. Electric field effect in atomically thin carbon films. *Science* **2004**, *306*, 666–669. [[CrossRef](#)] [[PubMed](#)]
- Yury, G. Transition metal carbides go 2D Nature Nanotechnology. *Nat. Mater.* **2015**, *14*, 1079–1080.
- Tian, H.W.; Liu, M.; Zheng, W.T. Constructing 2D graphitic carbon nitride nanosheets/layered MoS₂/graphene ternary nanojunction with enhanced photocatalytic activity. *Appl. Catal. B Environ.* **2018**, *225*, 468–476. [[CrossRef](#)]

4. Jariwala, D.; Sangwan, V.K.; Lauhon, L.J.; Marks, T.J.; Hersam, M.C. Emerging device applications for semiconducting two-dimensional transition metal dichalcogenides. *ACS Nano* **2014**, *8*, 1102–1122. [[CrossRef](#)] [[PubMed](#)]
5. Lin, B.; Li, H.; An, H.; Hao, W.B.; Wei, J.J.; Da, Y.Z.; Ma, C.S.; Yang, G.D. Preparation of 2D/2D g-C₃N₄ nanosheet@ZnIn₂S₄ nanoleaf heterojunctions with well-designed high-speed charge transfer nanochannels towards high-efficiency photocatalytic hydrogen evolution. *Appl. Catal. B Environ.* **2018**, *220*, 542–552. [[CrossRef](#)]
6. Lee, Y.T.; Jeon, P.J.; Han, J.H.; Ahn, J.; Lee, H.S.; Lim, J.Y.; Choi, W.K.; Song, J.D.; Park, M.; Lm, S.; et al. Mixed-Dimensional 1D ZnO-2D WSe₂ van der Waals Heterojunction Device for Photosensor. *Adv. Funct. Mater.* **2018**, *27*, 1703822–1703830. [[CrossRef](#)]
7. Yang, L.; Mao, M.; Zhou, B.B.; Tang, X.H.; Chen, C.; Ge, M.H.; Li, P.; Huang, X.J.; Yang, L.B.; Liu, J.H. Self-Assembled 2D Nanoparticles Arrays of interfacial self-assembled large-scale densely packed monolayer film with ligand exchanged Au nanorods for in situ SERS drugs detection. *Chem. A Eur. J.* **2018**, *24*, 1–10.
8. Chan, M.M.S.; Nie, W.; Stoumpos, C.C.; Tsai, H.; Blancon, J.; Liu, F.; Even, J.; Marks, T.J.; Mohite, A.D.; Kanatzidis, M.G. Understanding Film Formation Morphology and Orientation in High Member 2D Ruddlesden–Popper Perovskites for High-Efficiency Solar Cells. *Adv. Energy Mater.* **2017**, *8*, 1700979–1700989.
9. Atkin, P.; Daeneke, T.; Wang, Y.; Carey, B.J.; Berean, K.J.; Clark, R.M.; Ou, J.Z.; Trinchin, A.; Cole, I.S.; Kalantar-Zadeh, K. 2D WS₂/carbon dot hybrids with enhanced photocatalytic activity. *J. Mater. Chem. A* **2016**, *4*, 13563–13571. [[CrossRef](#)]
10. Ma, D.; Shi, J.W.; Zou, Y.; Zou, Y.J.; Fan, Z.Y.; Ji, X.; Niu, C. Highly Efficient Photocatalyst Based on a CdS Quantum Dots/ZnO Nanosheets 0D/2D Heterojunction for Hydrogen Evolution from Water Splitting. *ACS Appl. Mater. Interfaces* **2017**, *9*, 25377–25386. [[CrossRef](#)] [[PubMed](#)]
11. Yuan, Y.J.; Chen, D.; Zhong, J.S.; Yang, L.X.; Wang, J.J.; Liu, M.J.; Tu, W.G.; Yu, Z.T.; Zou, Z.G. Interface engineering of a noble-metal-free 2D–2D MoS₂/Cu-ZnIn₂S₄ photocatalyst for enhanced photocatalytic H₂ production. *J. Mater. Chem. A* **2017**, *5*, 15771–15779. [[CrossRef](#)]
12. Khan, A.F.; Down, M.P.; Smith, G.C.; Foster, C.W.; Banks, C.E. Surfactant-exfoliated 2D hexagonal boron nitride (2D-hBN): Role of surfactant upon the electrochemical reduction of oxygen and capacitance applications. *J. Mater. Chem. A* **2017**, *5*, 4103–4113. [[CrossRef](#)]
13. Oughaddou, H.; Enriquez, H.; Tchalala, M.R.; Yildirim, H.; Mayne, A.J.; Dujardin, A.; Bendounan, G.; Ali, M.A.; Kara, A. Silicene, a promising new 2D material. *Prog. Surf. Sci.* **2015**, *90*, 46–83. [[CrossRef](#)]
14. Singh, A.; Khare, P.; Verma, S.; Bhati, A.; Sonker, A.K.; Tripathi, K.M.; Sonkar, S.K. Pollutant Soot for Pollutant Dye Degradation: Soluble Graphene Nanosheets for Visible Light Induced Photodegradation of Methylene Blue. *ACS Sustain. Chem. Eng.* **2017**, *5*, 8860–8869. [[CrossRef](#)]
15. Miller, O.D.; Ilic, O.; Christensen, T.; Reid, M.T.H.; Atwater, H.A.; Joannopoulos, J.D.; Soljačić, M.; Johnson, S.G. Limits to the Optical Response of Graphene and Two-Dimensional Materials. *Nano Lett.* **2017**, *17*, 5408–5415. [[CrossRef](#)] [[PubMed](#)]
16. Cao, X.; Tian, G.; Chen, Y.; Zhou, J.; Zhou, W.; Tian, C.; Fu, H. Hierarchical composites of TiO₂ nanowire arrays on reduced graphene oxide nanosheets with enhanced photocatalytic hydrogen evolution performance. *J. Mater. Chem. A* **2014**, *2*, 4366–4374. [[CrossRef](#)]
17. Vidyasagar, D.; Ghugal, S.G.; Kulkarni, A.; Mishra, P.; Shende, A.G.; Jagannath; Umare, S.S.; Sasikala, R. Silver/Silver(II) oxide (Ag/AgO) loaded graphitic carbon nitride microspheres: An effective visible light active photocatalyst for degradation of acidic dyes and bacterial inactivation. *Appl. Catal. B Environ.* **2018**, *221*, 339–348. [[CrossRef](#)]
18. Giannakoudakis, D.A.; Arcibar-Orozco, J.A.; Bandosz, T.J. Effect of GO phase in Zn(OH)₂/GO composite on the extent of photocatalytic reactive adsorption of mustard gas surrogate. *Appl. Catal. B Environ.* **2016**, *183*, 37–46. [[CrossRef](#)]
19. Mady, A.H.; Baynosa, M.L.; Tuma, D.; Shim, J.J. Facile microwave-assisted green synthesis of Ag-ZnFe₂O₄@rGO nanocomposites for efficient removal of organic dyes under UV- and visible-light irradiation. *Appl. Catal. B Environ.* **2017**, *203*, 416–427. [[CrossRef](#)]
20. Tyagi, A.; Tripathi, K.M.; Singh, N.; Choudhary, S.; Gupta, R.K. Green synthesis of carbon quantum dots from lemon peel waste: Applications in sensing and photocatalysis. *RSC Adv.* **2016**, *6*, 72423–72432. [[CrossRef](#)]

21. Muhulet, A.; Miculescu, F.; Voicu, S.I.; Schütt, F.; Thakur, V.K.; Mishra, Y.M. Fundamentals and scopes of doped carbon nanotubes towards energy and biosensing applications. *Mater. Today Energy* **2018**, *9*, 154–186. [[CrossRef](#)]
22. Guo, Y.; Wang, H.; Ma, X.W.; Jin, J.; Ji, W.; Wang, X.; Song, W.; Zhao, B.; He, C.Y. Fabrication of Ag-Cu₂O/Reduced Graphene Oxide Nanocomposites as Surface-Enhanced Raman Scattering Substrates for in Situ Monitoring of Peroxidase-Like Catalytic Reaction and Biosensing. *ACS Appl. Mater. Interfaces* **2017**, *9*, 19074–19081. [[CrossRef](#)] [[PubMed](#)]
23. Lee, C.; Shin, K.; Lee, Y.J.; Jung, C.; Lee, H.M. Effects of shell thickness on Ag-Cu₂O core-shell nanoparticles with bumpy structures for enhancing photocatalytic activity and stability. *Catal. Today* **2017**, *303*, 313–319. [[CrossRef](#)]
24. Mishra, Y.K.; Adelung, R. ZnO tetrapod materials for functional applications. *Mater. Today* **2017**. [[CrossRef](#)]
25. Cheng, G.Q.; Wang, Y.; Liu, K.; Yu, J.H. Entropy-driven self-assembly of chiral nematic liquid crystalline phases of AgNR@Cu₂O hyper branched coaxial nanorods and thickness-dependent handedness transition. *Nano Res.* **2017**, *11*, 1018–1028. [[CrossRef](#)]
26. Wei, Y.J.; Wang, T.; Li, C.C.; Gong, J.J. A Low-Cost NiO Hole Transfer Layer for Ohmic Back Contact to Cu₂O for Photoelectrochemical Water Splitting. *Small* **2017**, *13*, 1702007–1702013. [[CrossRef](#)] [[PubMed](#)]
27. Marcano, D.C.; Kosynkin, D.V.; Berlin, J.M.; Sinitskii, A.; Sun, Z.; Slesarev, A.; Alemany, L.B.; Lu, W.; Tour, J.M. Improved Synthesis of Graphene Oxide. *ACS Nano* **2010**, *4*, 4806–4820. [[CrossRef](#)] [[PubMed](#)]
28. Chen, L.; Liu, M.M.; Zhao, Y.; Kou, Q.W.; Wang, Y.X.; Liu, Y.; Zhang, Y.J.; Yang, J.H.; Young, M.J. Enhanced Catalyst Activity by Decorating of Au on Ag@Cu₂O Nanoshell. *Appl. Surf. Sci.* **2018**, *435*, 72–78. [[CrossRef](#)]
29. Li, Y.; Cain, J.D.; Hanson, E.D.; Murthy, A.A.; Hao, S.Q.; Shi, F.G.; Li, Q.Q.; Wolverson, C.; Chen, X.Q.; Dravid, V.P. Au@MoS₂ Core–Shell Heterostructures with Strong Light–Matter Interactions. *Nano Lett.* **2016**, *16*, 7696–7702. [[CrossRef](#)] [[PubMed](#)]
30. Wang, B.S.; Li, R.Y.; Zhang, Z.Y.; Zhang, W.W.; Yan, X.L.; Wu, X.L.; Cheng, G.; Zheng, R.T. Novel Au/Cu₂O multi-shelled porous heterostructures for enhanced efficiency of photoelectrochemical water splitting. *J. Mater. Chem. A* **2017**, *5*, 14415–14421. [[CrossRef](#)]
31. Liang, X.; You, T.T.; Liu, D.P.; Lang, X.F.; Tan, E.Z.; Shi, J.H.; Yin, P.G.; Guo, L. Direct observation of enhanced plasmon-driven catalytic reaction activity of Au nanoparticles supported on reduced graphene oxides by SERS. *Phys. Chem.* **2015**, *17*, 10176–10181. [[CrossRef](#)] [[PubMed](#)]
32. Liang, X.; Liang, B.L.; Pan, Z.H.; Lang, X.F.; Zhang, Y.J.; Wang, G.S.; Yin, P.G.; Guo, L. Tuning plasmonic and chemical enhancement for SERS detection on graphene-based Au hybrids. *Nanoscale* **2015**, *7*, 20188–20196. [[CrossRef](#)] [[PubMed](#)]
33. Leong, K.H.; Lan, C.S.; Bahnemann, D.; Jang, M.; Lbrahim, S.; Saravanan, P. Reduced graphene oxide and Ag wrapped TiO₂ photocatalyst for enhanced visible light photocatalysis. *APL Mater.* **2015**, *6*, 20085–20092. [[CrossRef](#)]
34. Xiong, X.; Li, L.; Chen, J.; Zhang, S.; Wang, L.; Dou, S. Facile synthesis of highly efficient one-dimensional plasmonic photocatalysts through Ag@Cu₂O core-shell hetero-nanowires. *ACS Appl. Mater. Interfaces* **2014**, *6*, 15716–15725. [[CrossRef](#)] [[PubMed](#)]
35. Li, Y.F.; Yao, B.; Lu, Y.M.; Wei, Z.P.; Gai, Y.Q.; Zheng, C.J.; Li, B.H.; Shen, D.Z.; Fan, X.W.; Tang, Z.K. Realization of *p*-type conduction in undoped Mg_xZn_{1-x}O thin films by controlling Mg content. *Appl. Phys. Lett.* **2007**, *91*, 232115–232117. [[CrossRef](#)]
36. Xu, L.; Zhang, F.; Song, X.; Yin, Z.; Bu, Y. Construction of reduced graphene oxide-supported Ag–Cu₂O composites with hierarchical structures for enhanced photocatalytic activities and recyclability. *J. Mater. Chem. A* **2015**, *11*, 5923–5933. [[CrossRef](#)]

